Adv Syst Sci Appl 2024; **04**; 9-27
Published online at https://ijassa.ipu.ru.

Hall Current and Ion Slip Effects on 3D MHD Nanofluid Flow of Eyring-Powell Fluid with Gyrotactic Microorganisms

Murali Gundagani[1], Tan Kaun Tak[2], Sivaneasan Bala Krishnan[2], Pravin Kshirsagar[3], Venkata Madhu Javvaji[4]

[1)] *Geethanjali College of Engineering and Technology, Cheeryal, India*

[2)] *Singapore institute of Technology, Singapore*

[3)] *J.D. College of Engineering and Management, Nagpur, India*

[4)] *Sreenidhi Institute of Science and Technology, Yamnampet, India*

Abstract: This study explores the three-dimensional magnetohydrodynamic (MHD) flow of an Eyring-Powell nanofluid over a stretching sheet, incorporating the combined effects of Hall current, ion slip, gyrotactic microorganisms, thermal radiation, Brownian motion, thermophoresis, and key dimensionless parameters such as the Schmidt and Prandtl numbers. The investigation focuses on the practical applications of such flows, particularly in bioengineering and thermal systems, where magnetic fields and bio-convection play a crucial role. The governing equations are solved numerically using MATLAB's *bvp4c* solver, providing detailed insights into velocity profiles, temperature distribution, nanoparticle concentration, and microorganism density. Additionally, the study evaluates critical engineering parameters, including skin-friction coefficients, Nusselt number, Sherwood number, and motile microorganism density profiles. To ensure accuracy, the numerical method is validated against existing literature, confirming the reliability of the results. The findings offer valuable implications for enhancing heat and mass transfer in nanofluid-based technologies, thermal management systems, and bio-convective applications.

Keywords: Hall current; Three-dimensional; Nanofluid; Erying-Powell fluid; MHD; Hall current; Ion Slip; Stretching sheet; Gyrotactic Microorganisms.

1. INTRODUCTION

The study of gyrotactic microorganisms in a 3D nano-enhanced Eyring-Powell fluid flow over a stretching sheet, incorporating magnetohydrodynamics (MHD), Hall current, and ion slip effects, is motivated by its relevance to advanced bioengineering and thermal systems. Gyrotactic microorganisms play a crucial role in bio-convection, which enhances mixing and heat transfer in nanofluids, making them ideal for applications in biotechnology, medical diagnostics, and energy systems. The inclusion of MHD, Hall current, and ion slip effects addresses the influence of magnetic fields, which are pivotal in controlling fluid dynamics in industrial processes like magnetic drug targeting, microfluidic devices, and cooling systems for electronic equipment. This research provides insights into optimizing heat and mass transfer in complex fluid systems, offering potential advancements in biofuel production, wastewater treatment, and thermal management technologies. Research on Hall and ion slip effects in magnetohydrodynamic (MHD) flows highlights their critical role in altering flow dynamics and heat transfer. The Hall effect creates orthogonal electric fields from charged particles in magnetic fields, while ion slip reflects velocity differences between charged particles and neutral fluids. These effects, amplified by stronger magnetic fields, are vital for optimizing MHD systems.

Extensive research has explored these effects in various contexts. A strong magnetic field applied to an electric field generates an electric potential. This potential is derived from the Lorentz force created in charged gases, liquids, or electrically conductive fluids. For propagation to occur, it must go in a linear manner via the electric and magnetic fields. In

1879, Hall discovered this phenomenon and designated it as the "Hall effect" [1]. In some fluids, such as ionized gasses or conductive liquids, the Hall effect may alter the fluid's structure during flow due to the influence of magnetic orientation. The primary focus of the present study is the influence of Hall currents on the flow patterns of various nanofluids. Ions and charged particles traverse electromagnetic field lines, resulting in the electrodynamic phenomena referred to as Hall effect and ion-slip. The ion-slip current phenomena may often be disregarded, since ions possess far more mass than electrons and hence exhibit considerably slower movement. These events are very important when looking at the flow features of several problems. Das et al. [2] analyzed the Hall effects on the spontaneous nanofluid flow with thermal radiation. Krishna et al. [3] examined the Hall current effects on a water-based spinning nanofluid traversing a porous medium. Kumar et al. [4] investigated the influence of spinning and the Soret, Dufour, and Hall currents on magnetohydrodynamic flow in a porous media in their research. Bishnoi et al. [5] examined the influence of Hall currents on a magnetic nanofluid layer inside a continuous medium subjected to mono-diffusion. They accomplished this by supposing that the nanoparticles at the peripheries are passively organized. In reference [6], Swarnalathamma and colleagues examined the influence of Hall currents on a thick, incompressible fluid contained inside a porous media. Raghunath and Mohanaramana [7] examined the Soret effect on second-order fluids in rotation inside a porous media influenced by Hall currents in their work. Ji Le et al. [8] investigated the double-diffusive convection of a nanofluid inside a microchannel including Hall currents. Abbasi et al. examined the stability of electrically conducting nanofluids in the presence of Hall currents in their research [9]. The temperature instability of nanofluids under Hall currents in the Brinkman porous medium with no mass flux of nanoparticles at the edges was talked about in [10]. Some of the writers ([11], [12], [13], and [14]) looked into the Hall effect in MHD flow issues. These studies [15, 16, 17, 18, 19, and 20] do a great job of explaining what the Hall effect means for the flow of MHD nanofluid in a variety of geometrical shapes. A substantial body of additional research ([21]-[30]) further underscores the ongoing interest in understanding Hall and ion slip effects on rotating fluid flows past vertical surfaces.The authors conducted numerical analyses on various fluids, as referenced in [32]-[37]. These studies, combined with the extensive research outlined in [38]-[40] and [41]-[44], form a strong basis for the current investigation.

This study explores gyrotactic microorganism swimming in an Erying-Powell nanofluid near a stretching sheet, incorporating Hall current, ion slip, magnetic fields, thermal radiation, thermophoresis, and Brownian motion. Using MATLAB's "bvp4c," it numerically solves governing equations to analyze heat, mass, momentum, and microorganism density transfer. By examining parameter impacts on temperature, concentration, velocity, and microorganism profiles, the research aims to optimize flow dynamics and enhance design strategies for related applications.

2. MODELLING OF THE FLOW

In this current research work, the authors have examined 3-dimensional, Eyring-Powell fluid with nanofluid particles influenced by Thermal radiation, Gyrotactic microorganisms, Hall current, Ion slip, Thermophoresis, and Brownian motion on a non-conducting stretched sheet with Magnetic field. The following assumptions are used for this endeavour:

a) The fluid is electrically conducting in the presence of an applied magnetic field $B = \{0, 0, B_0\}$ is applied in the $z-$ direction.
b) Magnetic Reynolds number is assumed very small so that the induced magnetic field is ignored.
c) Let (u, v, w) be the velocity components along the (x, y, z) directions, respectively.
d) Flow is precipitated by a surface that is expanding at an exponential rate.

e) This means that the joint effects of diffusion are neglected into account when doing the calculations for energy and concentration, respectively.
f) When doing the calculation of concentration, the impact of chemical reaction is not taken into consideration.
g) In the section on boundary conditions, the influence of the many different slip effects is not taken into consideration.
h) The effects of Brownian motion and Thermophoresis are considered for nanofluid flow.
i) The effects of Hall current and Ion slips are considered in momentum equations.
j) The Cauchy stress tensor **T** is written as

$$\mathbf{T} = -pI + \tau \tag{1}$$

$$\rho a_i = -\nabla p + \nabla.\left(\tau_{ij}\right) + \sigma J \times B \tag{2}$$

where extra stress tensor τ_{ij} in an Eyring-Powell fluid model is

$$\tau_{ij} = \mu\left(\frac{\partial u_i}{\partial x_j}\right) + \frac{1}{\varepsilon}\sinh^{-1}\left(\frac{1}{c}.\frac{\partial u_i}{\partial x_j}\right) \tag{3}$$

Here ε and c are the characteristics of the Eyring-Powell fluid, p the pressure and I the identity tensor. Considering

$$\sinh^{-1}\left(\frac{1}{c}.\frac{\partial u_i}{\partial x_j}\right) \cong \frac{1}{c}.\frac{\partial u_i}{\partial x_j} - \frac{1}{6}\left(\frac{1}{c}.\frac{\partial u_i}{\partial x_j}\right)^3, \quad \left|\frac{1}{c}.\frac{\partial u_i}{\partial x_j}\right| \prec 1 \tag{4}$$

k) The modified generalized formula for Ohm's law is given, which takes into consideration the influences of Hall and ion slip at very high magnetic field strengths:

$$J = \sigma\left[E + \left(V \times B\right)\right] - \frac{\omega_e \tau_e}{B_o}\left(J \times B\right) + \frac{\omega_e \tau_e \beta_i}{B_o^2}\left[\left(J \times B\right) \times B\right] \tag{5}$$

By applying simplifications, Eq. (5) is reduced to

$$J_x = \sigma B_o\left[\frac{\beta_e u - \left(1 + \beta_e \beta_i\right) w}{\left(1 + \beta_e \beta_i\right)^2 + \beta_e^2}\right] \;\&\; J_z = \sigma B_o\left[\frac{\left(1 + \beta_e \beta_i\right) u + \beta_e w}{\left(1 + \beta_e \beta_i\right)^2 + \beta_e^2}\right] \tag{6}$$

The radiative heat flux q_r is defined as

$$q_r = -\frac{4\sigma^*}{3K^*}\left(\frac{\partial T^4}{\partial z}\right) \tag{7}$$

We assume that the temperature variances inside the flow are such that the term T^4 can be represented as linear function of temperature. This is accomplished by expanding T^4 in a Taylor series about a free stream temperature T_∞ as follows:

$$T^4 = T_\infty^4 + 4T_\infty^3\left(T - T_\infty\right) + 6T_\infty^2\left(T - T_\infty\right)^2 + \ldots\ldots\ldots \tag{8}$$

After neglecting higher-order terms in the above equation beyond the first-degree term in $\left(T - T_\infty\right)$, we get

$$T^4 \cong 4T_\infty^3 T - 3T_\infty^4 \tag{9}$$

Thus substituting Eq. (9) in Eq. (7), we get

$$q_r = -\frac{16T_\infty^3\sigma^*}{3K^*}\left(\frac{\partial T}{\partial z}\right) \tag{10}$$

The basic governing equations, continuity, momentum, energy, concentration, and microorganism equations, by applying the boundary layer approximations are

$$\frac{\partial u}{\partial x} + \frac{\partial v}{\partial y} + \frac{\partial w}{\partial z} = 0 \tag{11}$$

$$u\left(\frac{\partial u}{\partial x}\right)+v\left(\frac{\partial u}{\partial y}\right)+w\left(\frac{\partial u}{\partial z}\right)=\nu\left\{\left(\nu+\frac{1}{\rho\varepsilon C}\right)-\frac{1}{2\rho\varepsilon C^3}\left[\frac{\partial u}{\partial z}\right]^2\right\}\left(\frac{\partial^2 u}{\partial z^2}\right)-\left(\frac{\sigma B_o^2}{\rho}\right)\left[\frac{\left(1+\beta_e\beta_i\right)u+\beta_e w}{\left(1+\beta_e\beta_i\right)^2+\beta_e^2}\right] \tag{12}$$

$$u\left(\frac{\partial v}{\partial x}\right)+v\left(\frac{\partial v}{\partial y}\right)+w\left(\frac{\partial v}{\partial z}\right)=\nu\left\{\left(\nu+\frac{1}{\rho\varepsilon C}\right)-\frac{1}{2\rho\varepsilon C^3}\left[\frac{\partial v}{\partial z}\right]^2\right\}\left(\frac{\partial^2 v}{\partial z^2}\right)-\left(\frac{\sigma B_o^2}{\rho}\right)\left[\frac{\beta_e u-\left(1+\beta_e\beta_i\right)w}{\left(1+\beta_e\beta_i\right)^2+\beta_e^2}\right] \tag{13}$$

$$u\left(\frac{\partial T}{\partial x}\right)+v\left(\frac{\partial T}{\partial y}\right)+w\left(\frac{\partial T}{\partial z}\right)=\alpha\left(\frac{\partial^2 T}{\partial z^2}\right)+\tau_1\left\{D_B\left(\frac{\partial T}{\partial z}\right)\left(\frac{\partial C}{\partial z}\right)+\frac{D_T}{T_\infty}\left(\frac{\partial T}{\partial z}\right)^2\right\}+\frac{1}{\rho C_p}\left(\frac{16T_\infty^3\sigma^*}{3K^*}\right)\left(\frac{\partial^2 T}{\partial z^2}\right) \tag{14}$$

$$u\left(\frac{\partial C}{\partial x}\right)+v\left(\frac{\partial C}{\partial y}\right)+w\left(\frac{\partial C}{\partial z}\right)=D_B\left(\frac{\partial^2 C}{\partial z^2}\right)+\frac{D_T}{T_\infty}\left(\frac{\partial T}{\partial z}\right)^2 \tag{15}$$

$$u\left(\frac{\partial \chi}{\partial x}\right)+v\left(\frac{\partial \chi}{\partial y}\right)+\frac{b^* W_c}{\left(C_w-C_\infty\right)}\frac{\partial}{\partial y}\left(\chi\frac{\partial C}{\partial y}\right)=D_m\left(\frac{\partial^2 \chi}{\partial y^2}\right) \tag{16}$$

The boundary conditions for this flow are

$$\left.\begin{aligned}&u=u_w(x)=ax,\ v=v_w(y)=by,\ w=0,\ T=T_w,\ C=C_w,\ \chi=\chi_w\ \ at\ \ z=0\\&u\to 0,\ v\to 0,\ T\to T_\infty,\ C\to C_\infty,\ \chi\to\chi_\infty\ \ as\ \ z\to\infty\end{aligned}\right\} \tag{17}$$

Introducing the following similarity transformations

$$\left.\begin{aligned}&u=axf'(\eta),\ v=byg'(\eta),\ \phi=\frac{C-C_\infty}{C_w-C_\infty},\ w=-\sqrt{a\nu}\left\{f(\eta)+g(\eta)\right\},\\&\eta=\left(\sqrt{\frac{a}{\nu}}\right)z,\ \theta=\frac{T-T_\infty}{T_w-T_\infty},\ N=\frac{\chi-\chi_\infty}{\chi_w-\chi_\infty},\ u=\frac{\partial\psi}{\partial y},\ v=-\frac{\partial\psi}{\partial x},\end{aligned}\right\} \tag{18}$$

Making use of Eq. (18), Eqs. (12), (13), (14), (15) and (16) take the following form

$$\left(1+\varepsilon\right)f'''-\varepsilon\delta_1 f'''f''^2+ff''+gf''-f'^2-M^2f'-M^2\left[\frac{\left(1+\beta_e\beta_i\right)f'+\beta_e g'}{\left(1+\beta_e\beta_i\right)^2+\beta_e^2}\right]=0 \tag{19}$$

$$\left(1+\varepsilon\right)g'''-\varepsilon\delta_2 g'''g''^2+gg''+fg''-g'^2-M^2g'-M^2\left[\frac{\beta_e f'-\left(1+\beta_e\beta_i\right)g'}{\left(1+\beta_e\beta_i\right)^2+\beta_e^2}\right]=0 \tag{20}$$

$$\left(1+\frac{4}{3Nr}\right)\theta''+\Pr Nbf\theta'+\Pr Nbg\theta'+\Pr Nb\theta'\phi'+\Pr Nt\theta'^2=0 \tag{21}$$

$$Nb\phi''+NbScf\phi'+NbScg\phi'+Nt\theta''=0 \tag{22}$$

$$N''+LbfN'-PeN'\phi'+PeN\phi''+PeN\Omega=0 \tag{23}$$

the corresponding boundary conditions (10) become

$$\left.\begin{aligned}&f(0)=0,\ g(0)=0,\ f'(0)=1,\ g'(0)=\delta,\ \theta(0)=1,\ \phi(0)=1,\ N(0)=1,\\&f'(\infty)\to 0,\ g'(\infty)\to 0,\ \theta(\infty)\to 0,\ \phi(\infty)\to 0,\ N(\infty)\to 0\end{aligned}\right\} \tag{24}$$

where the involved physical parameters are defined as

$$\left.\begin{aligned}&M^2=\frac{\sigma B_o^2}{\rho a},\ Nb=\frac{\tau_1 D_B\left(C_w-C_\infty\right)}{\nu},\ Nt=\frac{\nu D_T\left(T_w-T_\infty\right)}{\nu T_\infty},\ Sc=\frac{\nu}{D_B},\ \Pr=\frac{\nu}{\alpha},\ \delta=\frac{b}{a},\ Nr=\frac{\kappa K^*}{4\sigma^* T_\infty^3},\\&\varepsilon=\frac{1}{\mu\beta C},\ \delta_1=\frac{a^3x^2}{2\nu C^2},\ \delta_2=\frac{a^3y^2}{2\nu C^2},\ Lb=\frac{\nu}{D_m},\ Pe=\frac{b^* W_c}{D_m},\ \Omega=\frac{N_\infty}{N_w-N_\infty},\end{aligned}\right\} \tag{25}$$

Quantities of physical interest, the physical parameters of the skin-friction coefficient along x and y - directions and local Nusselt number are presented as follows:

$$Cfx = C_f\left(\sqrt{\mathrm{Re}_x}\right) = \frac{\tau_{wx}}{\rho u_w^2} = \left\{(1+\varepsilon) f''(0) - \frac{1}{3}\varepsilon\delta_1 f''^3(0)\right\} \tag{26}$$

$$Cfy = C_f\left(\sqrt{\mathrm{Re}_y}\right) = \frac{\tau_{wy}}{\rho v_w^2} = \left\{(1+\varepsilon) g''(0) - \frac{1}{3}\varepsilon\delta_2 g''^3(0)\right\} \tag{27}$$

$$Nu = \frac{x q_w}{\kappa\left(T_w - T_\infty\right)} \tag{28}$$

where $q_w = -\kappa\left(\frac{\partial T}{\partial y}\right)_{y=0} + \left(q_r\right)_w \Rightarrow Nu = -\left(\sqrt{\mathrm{Re}_x}\right)\left(1+\frac{4}{3Nr}\right)\theta'(0)$

$$Sh = \frac{x q_m}{D_B\left(C_w - C_\infty\right)} = -\frac{x\left(\frac{\partial C}{\partial y}\right)_{y=0}}{D_B\left(C_w - C_\infty\right)} \Rightarrow Sh = -\left(\sqrt{\mathrm{Re}_x}\right)\phi'(0) \tag{29}$$

$$Nh = \frac{x d_w}{D_m\left(\chi_w - \chi_\infty\right)} = -\kappa\left(\frac{\partial \chi}{\partial y}\right)_{y=0} \Rightarrow \mathrm{Re}_x^{-\frac{1}{2}}\, Nh = -N'(0) \tag{30}$$

3.METHODS

The higher order nonlinear ordinary differential equations (ODEs) presented in equations (19) to (23) and the boundary conditions specified in equation (24) are solved numerically using the bvp4c solver available on the MATLAB computer platform. The bvp4c solver incorporates the three-stage Lobatto IIIA Runge-Kutta method, delivering numerical solutions with fourth-order precision. All subsequent steps have been executed to include the bvp4c solver into our physical model.

Step-1: New variables are introduced for the system of higher order non-linear ODEs in Eqs. (19)-(23).

$$\left.\begin{aligned} &y(1) = f,\ y(2) = f',\ y(3) = f'',\ y(4) = g,\ y(5) = g',\ y(6) = g'', \\ &y(7) = \theta,\ y(8) = \theta',\ y(9) = \phi,\ y(10) = \phi',\ y(11) = N,\ y(12) = N' \end{aligned}\right\} \tag{31}$$

Step-2: Reduce the system of higher order non-linear ODEs in Eqs. (19)-(23) to a system of first order non-linear ODEs using the new variables in Eq. (31).

$$f''' = \frac{\left\{-y(1)y(3) - y(4)y(3) + \left(y(2)\right)^2 + M^2 y(2) + M^2\left[\frac{\left(1+\beta_e\beta_i\right)y(2) + \beta_e y(5)}{\left(1+\beta_e\beta_i\right)^2 + \beta_e^2}\right]\right\}}{\left\{(1+\varepsilon) - \varepsilon\delta_1\left(y(3)\right)^2\right\}} \tag{32}$$

$$g''' = \frac{\left\{-y(4)y(6) - y(1)y(6) + \left(y(5)\right)^2 + M^2 y(5) + M^2\left[\frac{\beta_e y(2) - \left(1+\beta_e\beta_i\right)y(5)}{\left(1+\beta_e\beta_i\right)^2 + \beta_e^2}\right]\right\}}{\left\{(1+\varepsilon) - \varepsilon\delta_2\left(y(6)\right)^2\right\}} \tag{33}$$

$$\theta'' = \frac{\left\{-\mathrm{Pr}\,Nby(1)y(8) - \mathrm{Pr}\,Nby(4)y(8) - \mathrm{Pr}\,Nby(8)y(10) - \mathrm{Pr}\,Nt\left(y(8)\right)^2\right\}}{\left\{1+\frac{4}{3Nr}\right\}} \tag{34}$$

$$\phi'' = \frac{\left\{\begin{array}{l} -NbScy(1)\,y(10) - NbScy(4)\,y(10) \\ -ScNt\left\{\dfrac{\left\{\begin{array}{l} -\Pr Nby(1)\,y(8) - \Pr Nby(4)\,y(8) \\ -\Pr Nby(8)\,y(10) - \Pr Nt\left(y(8)\right)^2 \end{array}\right\}}{\left\{1+\dfrac{4}{3Nr}\right\}}\right\} \end{array}\right\}}{Nb} \tag{35}$$

$$N'' = -Lby(1)\,y(12) + Pey(10)\,y(12) - Pey(11)\Omega$$
$$-Pe\frac{y(11)}{Nb}\left\{-NbScy(1)\,y(10) - NbScy(4)\,y(10) - ScNt\left\{\frac{\left\{\begin{array}{l} -\Pr Nby(1)\,y(8) - \Pr Nby(4)\,y(8) \\ -\Pr Nby(8)\,y(10) - \Pr Nt\left(y(8)\right)^2 \end{array}\right\}}{\left\{1+\frac{4}{3Nr}\right\}}\right\}\right\} \tag{36}$$

Step-3: Express the boundary conditions in Eq. (24) in terms of the new variables in Eq. (31).

$$\left.\begin{array}{l} \left[y(1)\right]_p = 0,\ \left[y(4)\right]_p = 0,\ \left[y(2)\right]_p = 1,\ \left[y(5)\right]_p = \delta,\ \left[y(7)\right]_p = 1,\ \left[y(9)\right]_p = 1, \\ \left[y(2)\right]_q = 0,\ \left[y(5)\right]_q = 0,\ \left[y(7)\right]_q = 0,\ \left[y(9)\right]_q = 0,\ \left[y(11)\right]_p = 1,\ \left[y(12)\right]_q = 0, \end{array}\right\} \tag{37}$$

The subscripts 'p' and 'q' indicate the location the sheet at $\eta = 0$, and the location away from the sheet for a specific value of η. In this study, this location is set at $\eta = 3$ (for primary velocity profiles), $\eta = 4$ (for secondary velocity profiles), $\eta = 6$ (for temperature, concentration and microorganism profiles).

Step-4: The fourth phase involves using the bvp4c solver to implement the system of first-order non-linear ordinary differential equations specified by equations (32) to (36), together with the boundary conditions indicated in equation (37).

Step-5: Acquire the first and second solutions by using two separate sets of starting estimates sequentially while executing the bvp4c solver. This enables the acquisition of the primary and secondary solutions. If the computed temperature and velocity profiles conform to Equation (24), the initial estimates will be deemed acceptable; otherwise, this procedure will be replayed with a new set of initial guesses until the desired outcomes are attained. Typically, many attempts are required to get a suitable compilation of first observations.

Table-1.: Comparison of present Nusselt number coefficient results with published Nusselt number coefficient results of Hayat et al. [45] when, $\beta_e = \beta_i = \Omega = Sc = Nt = Nb = Pe = Lb = 0$.

M	Pr	Nr	ε	Hayat et al. [45] results	Present results
0.0	0.71	0.5	0.5	0.65496	0.664582750827
0.7				0.62357	0.610058625760
1.5				0.54949	0.539812850855
	1.0			0.59586	0.584574450825
	1.5			0.78096	0.774707605761
		1.0		0.41365	0.420656525663
		3.0		0.58315	0.580756545641
			0.7	0.57725	0.567775450852
			1.5	0.61980	0.608985976591

The authors have compared the present results of Nusselt number coefficient with published Nusselt number results of Hayat et al. [31] in absence of β_e, β_i, Ω, Sc, Nt, Nb, Pe, Lb. for different values of M, Pr, Nr, and ε in the table-1. From this table, it is observed that, the comparison results validated the accuracy as well as reliability of our computational approach by demonstrating excellent agreement with earlier studies.

4.RESULTS AND DISCUSSION

The purpose of the figures numbered 1 through 19 is to investigate the properties of non-dimensional primary and secondary velocity, temperature, concentration, and microorganism profiles across a variety of developmental parameters, including the following: These parameters include the Prandtl number (Pr), the thermal radiation parameter (Nr), the thermophoresis parameter (Nt), the Brownian motion parameter (Nb), the bio-convection Lewis number (Lb), the Peclet number (Pe), the microorganism difference parameter (Ω), the Schmidt number (Sc), the Erying-Powell fluid parameter (ε), the Hall current parameter (β_i), the ion slip parameter (β_e), the stretching sheet parameter (δ), and the magnetic field parameter (M^2). Calculated values of three engineering parameters, namely the mass transfer coefficient, the heat transfer rate coefficient, the skin-friction coefficient, and the motile density coefficient, are presented in Tables 2, 3, 4, 5, and 6. These values correspond to different values of the developmental parameters that were previously mentioned. It is of utmost importance to acknowledge that, unless otherwise specified in the graphs, the default parameter values that were used throughout the analysis were as follows: $M^2 = 0.3$, $\varepsilon = 0.5$, $\delta_1 = 0.5$, $\delta 2 = 0.5$, $\beta_e = 0.5$, $\beta_i = 0.5$, $\delta = 0.1$, $\lambda = 0.71$, $Nr = 0.5$, $Nb = 0.3$, $Nt = 0.5$, $Sc = 0.22$, $Lb = 0.5$, $Pe = 0.3$, and $\Omega = 0.4$. It can be seen in figures 1 and 2 that when the magnetic field parameter increases, the thickness of the boundary layer as well as the amplitudes of the main and secondary velocity profiles decrease. The current phenomenon is the physical outcome that occurs when an electric current travels through a conductive fluid when a magnetic field is present. The velocity of the fluid that is contained inside the boundary layer is therefore slowed down as a result of a drag force. Magnetic fields are no longer being used in any way, shape, or form. The main and secondary velocity profiles, as well as the Eyring-Powell fluid situation, were shown in Figures 3 and 4, respectively. According to the findings, there is a correlation between a rise in velocity profiles and an increase in the magnitude of the Eyring-Powell fluid values. Figures 5 and 6 illustrate the impact of the Hall parameter (β_e) on the velocity profiles of both the main and secondary components. By decreasing the effective electrical conductivity, the Hall parameter brings to a reduction in the magnitude of the magnetic resistive Lorentz force. Because of this, increased fluid dynamics are made possible, which ultimately results in an increase in both the main and secondary velocity profiles, as can be seen in Figures 7 and 8. A similar impact is exerted by the Ion slip parameter (β_i), as may be shown in Figures 9 and 10. Any rise in the values of the ion slip parameter results in a reduction in the damping or retarding force. The decrease in this damping force results in a rise in both the main and secondary velocity profiles simultaneously. The influence that the stretching ratio parameter has on the secondary velocity profiles is seen in Figure 11. It is observed that the secondary velocity profiles increase in proportion to the increasing value of the stretching rate ratio parameter. There is a correlation between the stretching parameter and the flow pressure, which often rises simultaneously. This is seen in Figure 12, which shows the temperature of the fluid in proportion to the Prandtl number. When the Prandtl number is increased, there is a decrease in the temperature gradient that the fluid is experiencing. Because of their lower thermal diffusivity, fluids that have a Prandtl number that is higher than that of the surrounding fluid exhibit lower temperatures. An illustration of the influence that the thermal radiation parameter, Nr, has on temperature profiles may be seen in Figure 13. An increase in the thermal radiation parameter results in a decrease in the temperature field. It is possible to see, in Figures 14 and 15, respectively, the impact that the Brownian motion parameter has on the temperature and concentration curves. According to the findings, an increase in the Brownian motion parameter results in a decrease in the concentration profile of nanoparticles and an increase in temperature. Brownian motion is the term used to describe the irregular movement of nanoparticles that are suspended in a fluid. This movement occurred as a consequence of interactions with the component particles of the fluid. As thermophoretic activity rises, Brownian motion also increases, which leads to an increase in temperature due

to the kinetic energy that is produced as a consequence. As can be seen in Figure 16, the Schmidt number, which is a dimensionless quantity that represents the ratio of momentum to mass diffusivity, has an effect on concentration patterns. In the concentration boundary layer, the calculation includes an evaluation of the relative mass and momentum transfer that occurs as a result of diffusion. Increasing the Schmidt number will result in a decrease in the mass diffusivity of the fluid, which will ultimately lead to a reduction in the concentration. Due to the fact that there is a negative connection between mass diffusivity and Schmidt number, the concentration boundary layers get thinner as the Schmidt number increases. An illustration of the impact that the bioconvection Lewis number has on the profiles of microorganisms may be seen in Figure 17. The diffusivity of microbial growth diminishes as the Lewis number increases owing to the decreasing population of microorganisms. Figure 18 illustrates how variations in the Peclet number may have an effect on the profiles of microorganisms. For the purpose of evaluating microbial profiles in connection to disease transmission, the Peclet number is the major measure that is used. Diffusion is the natural movement of particles from regions of higher concentration to regions of lower concentration. As the Peclet number increases, the diffusion density of the microorganisms decreases. The pattern shown in Figure 19 indicates that the evaluation of the microorganism differential parameter has risen, whilst the value of the microorganism profiles has diminished.

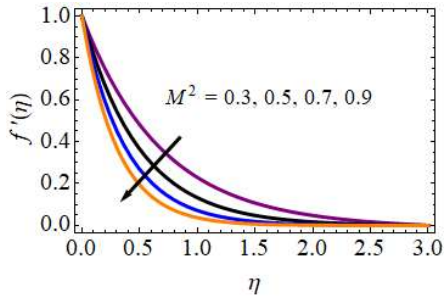

Fig. 1. The primary velocity profiles for different values of M^2.

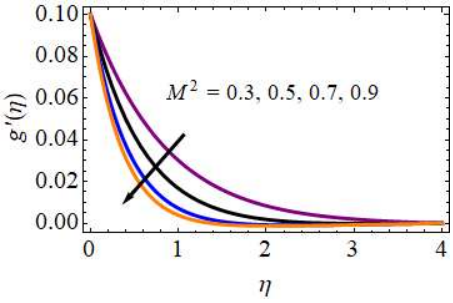

Fig. 2. The secondary velocity profiles for different values of M^2.

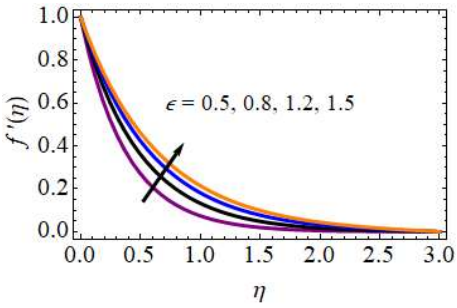

Fig. 3. The primary velocity profiles for different values of ε.

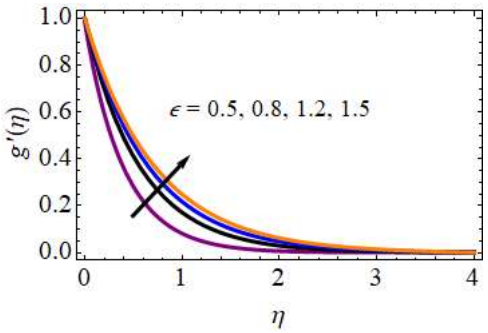

Fig. 4. The secondary velocity profiles for different values of ε.

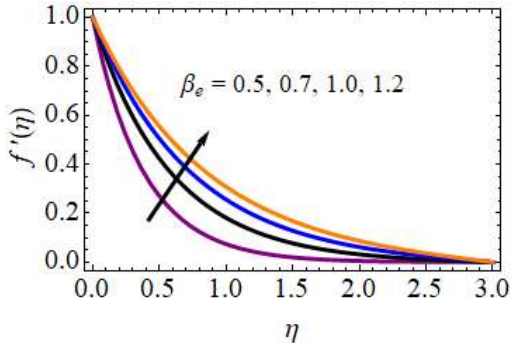

Fig. 5. The primary velocity profiles for different values of β_e.

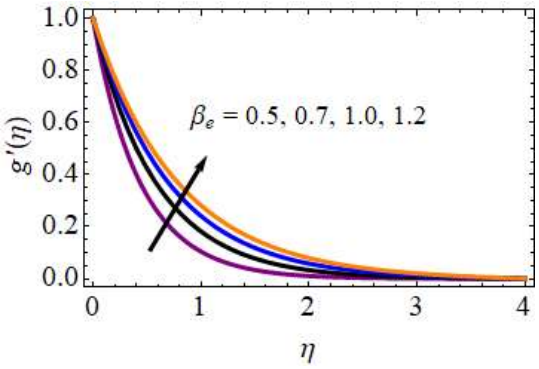

Fig. 6. The secondary velocity profiles for different values of β_e.

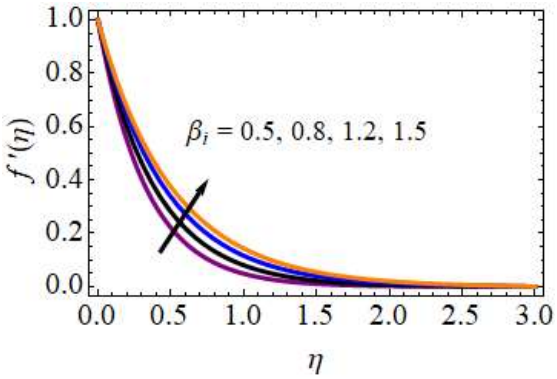

Fig. 7. The primary velocity profiles for different values of β_i.

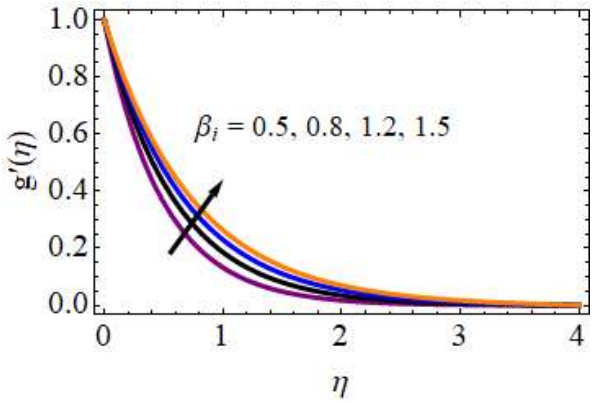

Fig. 8. The secondary velocity profiles for different values of β_i.

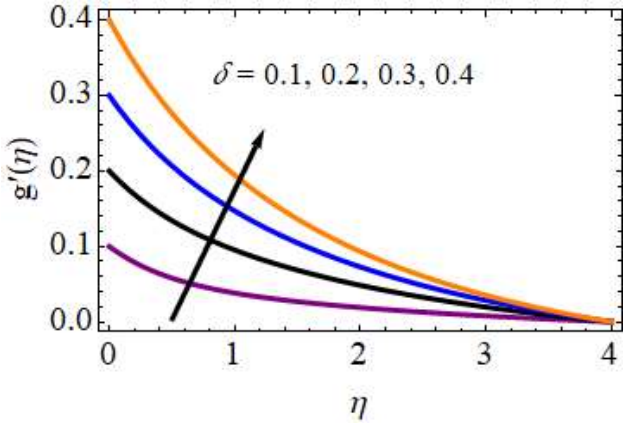

Fig. 9. The secondary velocity profiles for different values of δ.

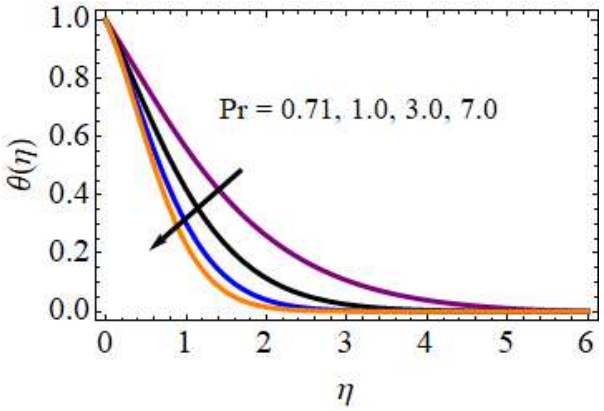

Fig. 10. The temperature profiles for different values of Pr.

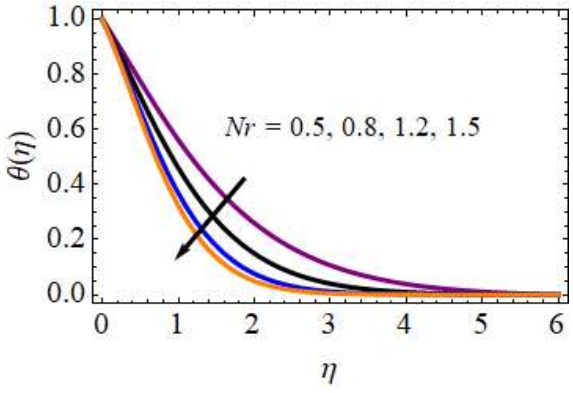

Fig. 11. The temperature profiles for different values of *Nr*.

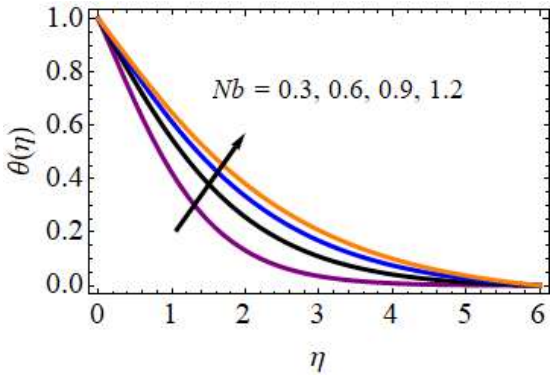

Fig. 12. The temperature profiles for different values of *Nb*.

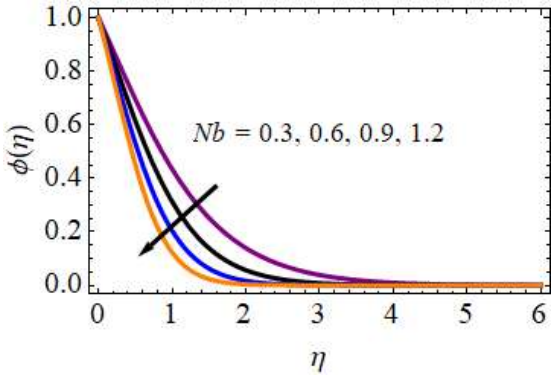

Fig. 13. The concentration profiles for different values of *Nb*.

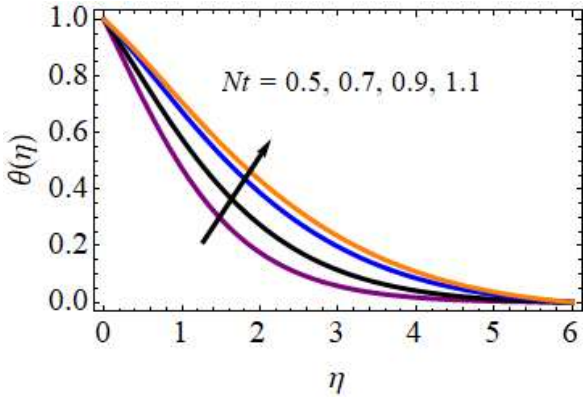

Fig. 14. The temperature profiles for different values of *Nt*.

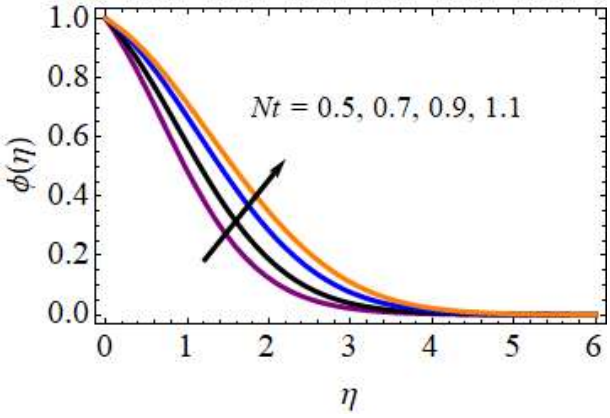

Fig. 15. The concentration profiles for different values of *Nt*.

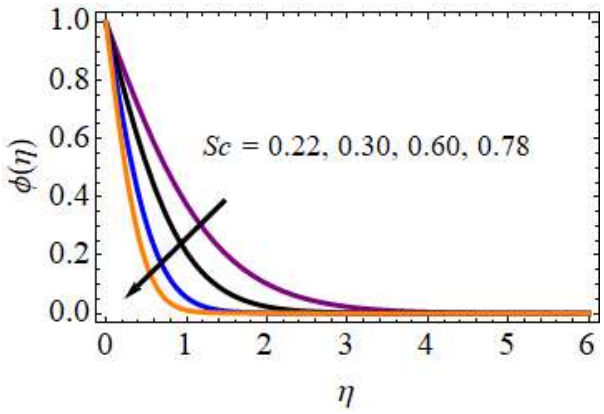

Fig. 16. The concentration profiles for different values of *Sc*.

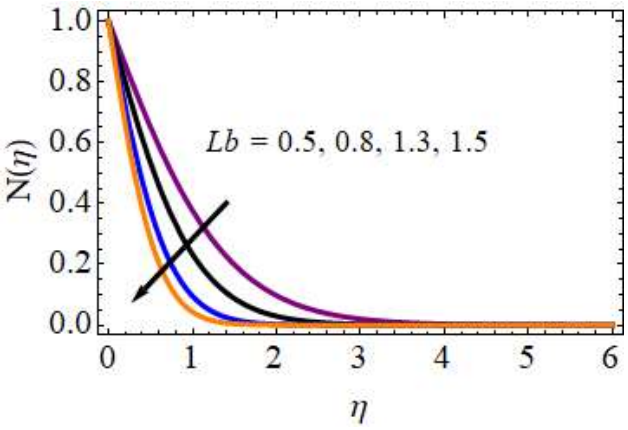

Fig. 17. The microorganism profiles for different values of *Lb*.

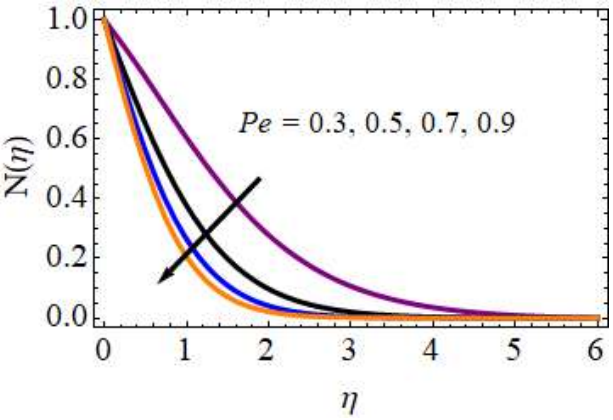

Fig. 18. The microorganism profiles for different values of *Pe*.

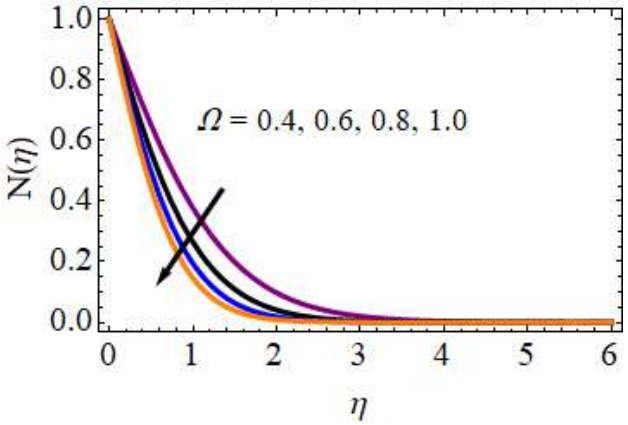

Fig. 19. The microorganism profiles for different values of Ω.

The variations in the values of engineering parameters, including the magnetic field parameter (M^2), the Erying-Powell fluid parameter (ε), the Hall current parameter (β_i), the Ion Slip parameter (β_e), the stretching sheet parameter (δ), the Prandtl number (Pr), the thermal radiation parameter (Nr), the thermophoresis parameter (Nt), the Brownian motion parameter (Nb), the bio-convection Lewis number (Lb), the Peclet number (Pe), the microorganism difference parameter (Ω), and the Schmidt number (Sc), influence the numerical values of the Skin-friction coefficients resulting from primary and secondary velocity profiles in the tables 2 and 3 respectively. The Skin-friction coefficients rise with increasing Erying-Powell fluid parameter (ε), Hall current parameter (β_i), Ion Slip parameter (β_e), Stretching sheet parameter (δ), Thermophoresis parameter (Nt), and Brownian motion parameter (Nb), while they decline with increasing Magnetic field parameter (M^2), Prandtl number (Pr), Thermal radiation parameter (Nr), Bio-convection Lewis number (Lb), Peclet number (Pe), Microorganism difference parameter (Ω), and Schmidt number (Sc).

Table 4 presents numerical values for the Nusselt number, or heat transfer coefficient, with the variable thermal radiation parameter (Nr), thermophoresis parameter (Nt), and Brownian motion parameter (Nb) throughout a spectrum of Prandtl numbers (Pr). The table demonstrates that the heat transfer coefficient progressively rises with elevated thermophoresis (Nt) and Brownian motion (Nb) parameters, while an inverse correlation is observed with increasing Prandtl number (Pr) and thermal radiation parameter (Nr). Table 5 examines the influence of the Schmidt number (Sc), Brownian motion parameter (Nb), and thermophoresis parameter (Nt) on the mass transfer coefficient rate. The mass transfer coefficient is represented by the Sherwood number, which corresponds to this table. The table indicates that when the Schmidt number (Sc) and Brownian motion parameter (Nb) increase, the mass transfer coefficient diminishes, however the thermophoresis parameter (Nt) escalates. The influence of Lb, Pe and Ω on mobile density coefficient is displayed in Table-6. From this table, it is noticed that the mobile density coefficient is decreasing with rising values of Lb, Pe and Ω.

Table-2.: Computed values of Skin-friction coefficient (Cfx)

M^2	ε	β_i	β_e	δ	Pr	Nr	Nb	Nt	Lb	Pe	Sc	Ω	Cfx
0.3	0.5	0.5	0.5	0.1	0.71	0.5	0.3	0.5	0.5	0.3	0.22	0.4	3.456583525815922
0.5													3.406061268620861
0.7													3.388658682619829
	0.8												3.486556276587343
	1.2												3.515768202865387
		0.8											3.474951668768258
		1.2											3.495668082562702
			0.7										3.495690226913641
			1.0										3.512545858650820
				0.2									3.486506133465045
				0.3									3.506061156506520
					1.00								3.415660441826508
					3.00								3.380066805656872
						0.8							3.426566252598689
						1.2							3.408745636498252
							0.6						3.476768467625982
							0.9						3.499679336561289
								0.7					3.496664206684765
								0.9					3.521534510825208
									0.8				3.415606252622856
									1.3				3.390656309642506
										0.5			3.426000109659652
										0.7			3.401324843645943
											0.30		3.415408658716259

											0.78		3.370526530927632
												0.6	3.425606256702650
												0.8	3.406657608764566

Table-3.: Computed values of Skin-friction coefficient (Cfy)

M^2	ε	β_i	β_e	δ	Pr	Nr	Nb	Nt	Lb	Pe	Sc	Ω	Cfy
0.3	0.5	0.5	0.5	0.1	0.71	0.5	0.3	0.5	0.5	0.3	0.22	0.4	1.352851541825180
0.5													1.326650369060196
0.7													1.306655425952255
	0.8												1.376650562106162
	1.2												1.390976896576576
		0.8											1.386750506916650
		1.2											1.402558764556252
			0.7										1.396750560165051
			1.0										1.413243865483424
				0.2									1.386576108650807
				0.3									1.406712956641965
					1.00								1.315454258528151
					3.00								1.296756063590165
						0.8							1.326502615760228
						1.2							1.306767561057671
							0.6						1.375610587618061
							0.9						1.396501365196316
								0.7					1.385618561672863
								0.9					1.405601566583027
									0.8				1.315606106059606
									1.3				1.285670601656275
										0.5			1.330006793647016
										0.7			1.315407562576860
											0.30		1.305345472383923
											0.78		1.284768545982564
												0.6	1.314360676452672
												0.8	1.296900162572027

Table-4.: Computed values of rate of heat transfer coefficient

Pr	Nb	Nt	Nr	Nu
0.71	0.3	0.5	0.5	1.657056171845669
1.00				1.629752354986598
3.00				1.601407253852805
	0.6			1.684502650187268
	0.9			1.704558025828522
		0.7		1.694524835108735
		0.9		1.710764651925378
			0.8	1.624645685423892
			1.2	1.608576265038681

Table-5.: Computed values of rate of mass transfer coefficient

Nb	Nt	Sc	Sh
0.3	0.5	0.22	2.154692359825368
0.6			2.085802530876287
0.9			2.050062352635852
	0.7		2.185023654625034
	0.9		2.210523854026982
		0.30	2.058756087650268
		0.78	2.001542083581751

Table-6.: Computed values of Motile density coefficient

Lb	*Pe*	*Ω*	*Nh*
0.5	0.3	0.4	2.515876257825823
0.8			2.480570257602762
1.3			2.451472085612873
	0.5		2.496906962396209
	0.7		2.471545585283523
		0.6	2.470560162569676
		0.8	2.450650276357892

5.CONCLUSIONS

The impacts of the Hall current and Ion slip current on three-dimensional, incompressible, viscous, electrically conducting, steady, radiating, MHD flow of the Nano + Powell-Erying fluid past a stretching sheet by means of swimming of microorganisms. The concluding remarkable points are represented as of the subsequent.

- The study shows that both primary and secondary velocity profiles decrease with an increase in the magnetic field number, while it increases with higher values of the Hall parameter, Ion Slip parameter, Powell-Erying fluid parameter.
- The temperature distribution decreases as the Prandtl number and Thermal radiation parameter increases but rises with an increase in the Thermophoresis parameter and Brownian motion parameter.
- For concentration, an increase in the Thermophoresis parameter enhances the concentration distribution, whereas an increase in the Schmidt number and Brownian motion parameter decreases it.
- Finally, the numerical results obtained are ultimately more precise in comparison to the published findings of Hayat et al. [45] in absence of β_e, β_i, Ω, *Sc*, *Nt, Nb, Pe*, *Lb* for different values of *M*, Pr, *Nr*, and ε.

ACKNOWLDGEMENT

This work was conducted as part of my postdoctoral research at the Singapore Institute of Technology (SIT). I gratefully acknowledge SIT for its support and extend my sincere thanks to my postdoctoral supervisor, Dr. Tan Kaun Tak, and the co-PIs for their invaluable guidance. I also appreciate the resources provided by the Power and Energy Lab and the stimulating discussions with colleagues.

REFERENCES

[1] Alamirew, W. D., Zergaw, G. A. & Gorfie, E. H. (2024). Effects of Hall, ion slip, viscous dissipation and nonlinear thermal radiation on MHD Williamson nanofluid flow past a stretching sheet, *International Journal of Thermofluids*, **22**, 100646 doi: 10.1016/j.ijft.2024.100646

[2] RamReddy, C., Surender, O. & Venkata Rao, C. (2016). Effects of Soret, Hall and Ion-slip on mixed convection in an electrically conducting Casson fluid in a vertical channel, *Nonlinear Engineering*, **5**(3), 167-175. doi: 10.1515/nleng-2016-0023

[3] Rajakumar, K., Umasankara Reddy, M., Balamurugan, K. & Raja Ram, K. (2020). Steady MHD Casson ohmic heating and viscous dissipative fluid flow past an infinite vertical porous plate in the presence of Soret, Hall, and ion-slip current, *Heat Transfer*, **49**(3), 1583-1612. doi: 10.1002/htj.21693

[4] Ibrahim, W. & Anbessa, T. (2020). Three-dimensional MHD mixed convection flow of Casson nanofluid with Hall and ion slip effects, *Mathematical Problems in Engineering*, **2020**, 1-15.
doi: 10.1155/2020/8656147

[5] Kumar, D., Kolapati, B. S. L. & Kandi, R. (2023). Effects of Hall current and activation energy on a three-dimensional rotating Casson hybrid nanofluid flow over a stretched plate in the presence of Joule heating and nonlinear thermal radiation, *Journal of Advanced Research in Fluid Mechanics and Thermal Sciences*, **109**(1), 51-70.
doi: 10.37934/arfmts.109.1.5170

[6] Suresh Kumar, Y., Hussain, S., Raghunath, K., Ali, F., Guedri, K., et al. (2023). Numerical analysis of magnetohydrodynamics Casson nanofluid flow with activation energy, Hall current and thermal radiation, *Scientific Reports*, **13**(1), 4021.
doi: 10.1038/s41598-023-31190-x

[7] Ibrahim, W. & Anbessa, T. (2019). Mixed convection flow of nanofluid with Hall and ion-slip effects using spectral relaxation method, *Journal of the Egyptian Mathematical Society*, **27**(1), 1-21.
doi: 10.1186/s42787-019-0005-1

[8] Krishna, M. V., Ahamad, N. A. & Chamkha, A. J. (2021). Hall and ion slip impacts on unsteady MHD convective rotating flow of heat generating/absorbing second grade fluid, *Alexandria Engineering Journal*, **60**(1), 845-858.
doi: 10.1016/j.aej.2020.10.013

[9] Seddeek, M. (2001). Effects of Hall and ion-slip currents on magneto-micropolar fluid and heat transfer over a non-isothermal stretching sheet with suction and blowing, *Proceedings of the Royal Society A: Mathematical, Physical and Engineering Sciences*, **457**(2016), 3039-3050.
doi: 10.1098/rspa.2001.0824

[10] Krishna, M. V. (2021). Hall and ion slip effects on radiative MHD rotating flow of Jeffreys fluid past an infinite vertical flat porous surface with ramped wall velocity and temperature, *International Communications in Heat and Mass Transfer*, **126**, 105399.
doi: 10.1016/j.icheatmasstransfer.2021.105399

[11] Ayub, A., Asjad, M. I., Al-Malki, M. A. S., Khan, S., Eldin, S. M., et al. (2024). Scrutiny of nanoscale heat transport with ion-slip and Hall current on ternary MHD cross nanofluid over heated rotating geometry, *Case Studies in Thermal Engineering*, 53, 103833.
doi: 10.1016/j.csite.2024.103833

[12] Akram, M., Ala'yed, O., Saadeh, R., Qazza, A., Obalalu, A. M., et al. (2024). Exploring the dynamic behavior of the two-phase model in radiative non-Newtonian nanofluid flow with Hall current and ion slip effects, *Journal of Radiation Research and Applied Sciences*, **17**(4), 101112.
doi: 10.1016/j.jrras.2024.101112

[13] Alamirew, W. D., Zergaw, G. A. & Gorfie, E. H. (2024). Effects of Hall, ion slip, viscous dissipation and nonlinear thermal radiation on MHD Williamson nanofluid flow past a stretching sheet, *International Journal of Thermofluids*, **22**, 100646.
doi: 10.1016/j.ijft.2024.100646

[14] Alamirew, W. D., Awgichew, G. & Haile, E. (2024). Mixed Convection Flow of MHD Casson Nanofluid over a Vertically Extending Sheet with Effects of Hall, Ion Slip and Nonlinear Thermal Radiation, *International Journal of Thermofluids*, **23**, 100762.
doi: 10.1016/j.ijft.2024.100762

[15] Krishna, M. V. (2025). Diffusion-thermo, Thermo-diffusion, Hall and ion slip effects on MHD flow through porous medium in a rotating channel, *Chemical Physics*, 112623.
doi: 10.1016/j.chemphys.2025.112623

[16] Krishna, M. V. & Chamkha, A. J. (2019). Hall and ion slip effects on MHD rotating boundary layer flow of nanofluid past an infinite vertical plate embedded in a porous medium, *Results in Physics*, **15**, 102652.
doi: 10.1016/j.rinp.2019.102652

[17] Krishna, M. V. & Rajasekhar, E. (2024). Extreme electromagnetic rotation, chemical reaction, Hall and ion slip effects on weakly ionized fluid in a Riga channel, *Results in Engineering*, **24**, 103169.
doi: 10.1016/j.rineng.2024.103169

[18] Khan, Z. H., Makinde, O. D., Ahmad, R. & Khan, W. A. (2018). Numerical study of unsteady MHD flow and entropy generation in a rotating permeable channel with Slip and Hall effects, *Communications in Theoretical Physics*, **70**(5), 641-650.
doi: 10.1088/0253-6102/70/5/641

[19] Krishna, M. V., Ahamad, N. A. & Chamkha, A. J. (2021). Hall and ion slip impacts on unsteady MHD convective rotating flow of heat generating/absorbing second grade fluid, *Alexandria Engineering Journal*, **60**, 845-858.
doi: 10.1016/j.aej.2020.10.013

[20] Krishna, M. V., Ahamad, N. A. & Aljohani, A. F. (2021). Thermal radiation, Chemical reaction, Hall and Ion slip effects on MHD oscillatory rotating flow of micro-polar liquid, *Alexandria Engineering Journal*, **60**, 3467-3484.
doi: 10.1016/j.aej.2021.02.010

[21] Krishna, M. V. (2021). Radiation-absorption, chemical reaction, Hall and ion slip impacts on magnetohydrodynamic free convective flow over semi-infinite moving absorbent surface, *Chinese Journal of Chemical Engineering*, **34**, 40-52.
doi: 10.1016/j.cjche.2020.12.026

[22] Kanimozhi, N., Vijayaragavan, R. & Shanmugam, K. (2022). Impacts of thermal radiation, viscous dissipation, ohmic heating, and diffusion-thermo effects on unsteady MHD free convective rotating flow of second-grade fluid with Hall and ion-slip currents, *Heat Transfer*, **51**, 7435-7461.
doi: 10.1002/htj.22651

[23] Das, S., Ali, A. & Jana, R. N. (2020). Impact of Hall currents with buoyancy forces on hydromagnetic reactive Casson fluid flow past a slippery plate in a rotating porous medium, *Special Topics & Reviews in Porous Media - An International Journal*, **11**(4), 313-340.
DOI: 10.1615/SpecialTopicsRevPorousMedia.2020033661

[24] Krishna, M. V. (2021). Hall and ion slip effects on the MHD flow of Casson hybrid nanofluid past an infinite exponentially accelerated vertical porous surface, *Waves in Random and Complex Media*, doi: 10.1080/17455030.2021.1998727

[25] Islam, M., Nasrin, S. & Alam, M. (2022). Unsteady MHD fluid flow over an inclined plate, inclined magnetic field and variable temperature with Hall and ion-slip current, *Ricerche di Matematica*.
DOI: 10.1007/s11587-022-00728-y

[26] Kumar, S. & Ibrahim, S. (2022). Cubic B-splines method for Hall and ion slip impacts on unsteady MHD rotating flow past a vertical moving porous plate, *Heat Transfer*, **51**, 3620-3635.
DOI: 10.1002/htj.22467

[27] Krishna, M. V. (2022). Hall and ion slip effects and chemical reaction on MHD rotating convective flow past an infinite vertical porous plate with ramped wall and uniform wall temperatures, *Biomass Conversion and Biorefinery*.
DOI: 10.1007/s13399-022-03160-2

[28] Uddin, Z. & Kumar, M. (2013). Hall and ion-slip effect on MHD boundary layer flow of a micro polar fluid past a wedge, *Scientia Iranica B*, **20**(3), 467-476.
DOI: 10.1016/j.scient.2013.02.013

[29] Ellahi, R., Bhatti, M. M. & Pop, I. (2016). Effects of Hall and ion slip on MHD peristaltic flow of Jeffrey fluid in a non-uniform rectangular duct, *International Journal of Numerical Methods for Heat & Fluid Flow*, **26**(6), 1802-1820. doi: 10.1108/HFF-02-2015-0045

[30] Bhatti, M. M., Abbas, M. A. & Rashidi, M. M. (2016). Effect of Hall and ion slip on peristaltic blood flow of Eyring Powell fluid in a non-uniform porous channel, *World Journal of Modelling and Simulation*, **12**(4), 268-279.

[31] Babu, N. V. N., Murali, G. & Bhati, S. M. (2018). Casson fluid performance on natural convective dissipative couette flow past an infinite vertically inclined plate filled in porous medium with heat transfer, MHD and hall current effects, *International Journal of Pharmaceutical Research*, **10**(4), 809-819.

[32] Kirubaharan, D. R., Subhashini, A. D. & Murali, G. (2024). Study of Three Dimensional Casson-Nanofluid Flow due to a Linear Porous Stretching Sheet in the Presence of Double Diffusion Effects, *Advances in Systems Science and Applications*, **24**(3), 90-103. doi: 10.25728/assa.2024.2024.03.1539

[33] Gundagani, M., Babu, N. V. N., GadPally, D., Bhati, S.M., Sanjay, Ch, et al. (2024). Study of Nano-Powell-Erying fluid flow past a porous stretching sheet by the effects of MHD, thermal and mass convective boundary conditions, *Journal of Umm Al-Qura University for Engineering and Architecture*, **15**, 271-281. doi: 10.1007/s43995-024-00056-2

[34] Gundagani, M., Mamidi, L.P. & Tanuku, P.K. (2024). Finite element solutions of Double diffusion effects on three-dimensional MHD Nano-Powell-Erying fluid flow in presence of thermal and mass Biot numbers, *Journal of Engineering and Applied Science*, **71**, 9. doi: 10.1186/s44147-023-00347-w

[35] Murali, G., Deepa, G., Venkata Madhu, J., Nirmala Kasturi, V., Bhati, S.M., (2025). Three Dimensional Chemically Reacting Oldroyd-B Fluid + Nanofluid Flow in Presence of Thermophoresis and Brownian Motion Effects, *Discontinuity, Nonlinearity, and Complexity*, **14**(2), 373-388. doi: 10.5890/DNC.2025.06.010

[36] Murali, G., Deepa, G., Nirmala Kasturi, V. & Poornakantha, T. (2023). Joint effects of thermal diffusion and diffusion thermo on MHD three dimensional nanofluid flow towards a stretching sheet, *Mathematical Models in Engineering*, **9**(4), 130-143. doi: 10.21595/mme.2023.23590

[37] Murali, G., Babu, N. V. N., Convective MHD Jeffrey Fluid Flow Due to Vertical Plates with Pulsed Fluid Suction: A Numerical Study, *Journal of Computational Applied Mechanics*, 54 (1), 36-48, 2023. https://jcamech.ut.ac.ir/article_90604.html

[38] Bhati, S. M., Murali, G. & Sanjay, Ch. (2022). Law of elecric fields via bianchi identities, *Journal of Applied Science and Engineering*, **25**(4), 759-762. doi: 10.6180/jase.202208_25(4).0011

[39] Tanuku, P. K., Mamidi, L. P. & Gundagani, M. (2024). Modelling and analysis of three-dimensional chemically reacting, radiating Casson-nanofluid flow: thermophoresis and Brownian motion effects, *Acta Polytechnica*, **64**(5), 455-463. doi: 10.14311/AP.2024.64.0455

[40] Poornakantha, T., Laksmiprsanna, M. & Murali, G. (2025). Modelling and Analysis of Three-Dimensional Maxwell-Nanofluid Flow over a Bi-Directional Stretching Surface in the Presence of a Magnetic Field. *International Journal for Engineering Modelling,* **38**(1), 53-72 doi: 10.31534/engmod.2025.1.ri.04d.

[41] Singh, N., Kaur, J., Thakur, P. & Murali, G. (2023). Structural behaviour of annular isotropic disk made of steel/copper material with gradually varying thickness subjected to internal pressure, *Structural Integrity and Life*, **23**(3), 293-297.

[42] Sivaiah, S., Gundagani, M. & Karanamu, M. P. (2012) Analysis of Heat and Mass Transfer Effects on an Isothermal Vertical Oscillating Plate, *Walailak Journal of Science and Technology*, **9**(4), 407-415.

[43] Murali, G., Venkata Madhu, J., Deepa, G., Suresh, P. & Nagaraju, B. (2025). Three-Dimensional Oldroyd-B Fluid Flow Past a Stretching Surface with Magnetic Field, Nanofluid Particles and Cattaneo-Christov Double Diffusion Effects, *Johnson Matthey Technology Review*, **69**(2), 299-320.
doi: 10.1595

[44] Hayat, T., Awais, M. & Asghar, S. (2013). Radiative effects in a three-dimensional flow of MHD Eyring-Powell fluid, *Journal of the Egyptian Mathematical Society*, **21**, 379-384.
doi: 10.1016/j.joems.2013.03.003

